

## Testing models of accreting stars in massive binaries on $\zeta$ Ophiuchi

M. RENZO<sup>1,2</sup> AND Y. GÖTBERG<sup>3</sup>

<sup>1</sup>*Department of Physics, Columbia University, New York, NY 10027, USA*

<sup>2</sup>*Center for Computational Astrophysics, Flatiron Institute, New York, NY 10010, USA*

<sup>3</sup>*The Observatories of the Carnegie Institution for Science, 813 Santa Barbara Street, Pasadena, CA 91101, USA*

### ABSTRACT

Binarity dominates the evolution of massive stars, and the nearest O-type star to Earth,  $\zeta$  Ophiuchi, has long been proposed to be a product of binary evolution. Despite this, most stellar models have tried unsuccessfully to reproduce its observable properties relying on single-star rotating models. ■ **[Here we do better]** ■

*Keywords:* stars: individual:  $\zeta$  Ophiuchi – stars: massive – stars: binaries

### 1. INTRODUCTION

The overwhelming majority of massive stars is born in multiple systems (e.g., Mason et al. 2009; Almeida et al. 2017), and a large fraction will exchange mass or merge with a companion in their lifetime (e.g., Sana et al. 2012). The most common type of interaction is a post-main-sequence stable mass transfer (case B) through Roche Lobe overflow (RLOF, Kippenhahn & Weigert 1967, ■ **[pop synth. ref.]** ■. Many studies (e.g. Götzberg et al. 2017, 2018; Laplace et al. 2020, 2021) have focused on the dramatic impact of these interactions on the donor star, often treating the closest binary companion as a point mass. ■ **[more refs, other groups]** ■

However, binary interactions have a crucial impact on the secondary star too. Because of mass transfer, these are expected to accrete mass and rejuvenate because of the accompanying growth of the convective core (e.g., Neo et al. 1977; Schneider et al. 2016), spin up to critical rotation (e.g., Packet 1981; Cantiello et al. 2007), and possibly be polluted by CNO-processed material from the inner core of the donor star (e.g., Blaauw 1993).

Understanding the evolution of accretors in massive binaries has wider and crucial implications for stellar populations, electromagnetic transient observations, and gravitational-wave progenitors. Binary products, and accretors in particular, can impact cluster populations and their age estimates and main sequence morphology (e.g., Pols & Marinus 1994; Wang et al. 2020). Moreover, the majority of massive binaries will be disrupted by the first supernova ejecting the companion (“binary SN scenario”, Blaauw 1961; De Donder et al. 1997; Eldridge et al. 2011; Renzo et al. 2019; Evans et al. 2020). Therefore, populations of field massive stars con-

tain presently single O-type stars that accreted mass earlier on. The majority of these will be too slow to stand out in astrometric surveys (e.g., Eldridge et al. 2011; Renzo et al. 2019). Assuming a constant star formation history, Renzo et al. (2019) estimated that  $10.1^{+4.6}_{-8.6}\%$  of O-type stars might be accretors released after a SN – where the errors span a range of parameter variations.

From the transients perspective, accretors stars are also important: Zapartas et al. (2019) showed that  $14^{+4}_{-11}\%$  of hydrogen-rich (type II) SNe might come from these progenitors after being ejected from a binary. The fact that they accreted mass before exploding can influence their helium (He) core mass and thus the explosion properties and the inferred progenitors (Zapartas et al. 2021).

Finally, the majority of isolated binary evolutionary scenarios for gravitational-wave progenitors go through a common-envelope phase initiated by the originally less massive accretor after the formation of the first compact object (e.g., Belczynski et al. 2016; Tauris et al. 2017; Broekgaarden et al. 2021). Therefore, it is possible that accretion of mass before the formation of the first compact object could modify the internal structure of the star that will initiate the common-envelope phase (e.g. Law-Smith et al. 2020; Klencki et al. 2021).

Despite their importance, accretor stars in binaries have so far received much less attention than the donor stars, with the pioneering work of Hellings (1983, 1984) and Braun & Langer (1995) as notable exceptions. Large grids of accretor models are lacking, most of the studies focus on lower mass B-type donors (e.g., van Rensbergen et al. 2006, 2011, but see also Wang et al. 2020) and only few sparse massive models exist (e.g., Cantiello et al. 2007). This is because of the complexity

of these models, where one needs to follow in detail the *coupled* evolution of two rotating stars exchanging mass. Moreover, the admittedly large number of free parameters involved in the modeling of each individual star and their interactions makes robust predictions challenging to obtain. Here, we will argue that the nearest O-type star to Earth,  $\zeta$  Ophiuchi<sup>1</sup> ( $\zeta$  Oph) provides a unique opportunity to constrain these models.

$\zeta$  Oph has a distance from Earth of  $107 \pm 4$  pc (Neuhäuser et al. 2020, and references therein), and a spectral type O9.5IVnn (Sota et al. 2014). It occasionally shows emission lines (Walker et al. 1979; Vink et al. 2009), making it an Oe star. It was originally identified as a runaway because of its large proper motion by Blaauw (1952). Unfortunately, the *Gaia* data for this object are not of sufficient quality<sup>2</sup> to improve previous astrometric results, but estimates of the peculiar velocity range in  $30 - 50$  km s<sup>-1</sup> (e.g., Zehe et al. 2018; Neuhäuser et al. 2020). The large velocity with respect to the surrounding interstellar material is also confirmed by the presence of a prominent bow-shock (e.g., Bodensteiner et al. 2018).

Because of its young apparent age, extremely fast rotation ( $v \sin(i) \gtrsim 400$  km s<sup>-1</sup>, e.g., Zehe et al. 2018), and nitrogen (N) and He rich surface (e.g., Herrero et al. 1992; Blaauw 1993; Villamariz & Herrero 2005; Marcolino et al. 2009),  $\zeta$  Oph is a prime candidate for the binary SN scenario (Blaauw 1993). Many studies have suggested  $\zeta$  Oph might have accreted mass from a companion before acquiring its large velocity, both from spectroscopic and kinematic considerations (e.g., Blaauw 1993; Hoogerwerf et al. 2000, 2001; Tetzlaff et al. 2010; Neuhäuser et al. 2020) and using stellar modeling arguments (e.g., van Rensbergen et al. 1996). Recently, Neuhäuser et al. (2020) suggested that a supernova in Upper-Centaurus-Lupus produced the pulsar PSR B1706-16, ejected  $\zeta$  Oph, and also injected the short-lived radioactive isotope <sup>60</sup>Fe on Earth  $1.78 \pm 0.21$  Myr ago. This argues strongly for a successful supernova explosion accompanied by a large  $\sim 250$  km s<sup>-1</sup> natal kick, which in most cases would be sufficient to disrupt the binary.

Although the nature of  $\zeta$  Oph as a binary product is well established, its observed large surface rotation rate has lead previous attempts to rely on rotational mixing to explain the surface composition (e.g., Maeder & Meynet 2000). Even the binary models of van Rensbergen et al. (1996) assumed spin-up due to mass accretion

to drive rotational mixing from the interior of the accreting star (see also Cantiello et al. 2007). However, Villamariz & Herrero (2005) (hereafter, VH05) were unable to find good fit for the stellar spectra using the rotating models from Meynet & Maeder (2000).

This may not be surprising: rotational mixing has lower efficiency for metal-rich and relatively low mass stars because of the increased importance of mean molecular weight gradients and longer thermal timescales compared to more massive stars (e.g., Yoon et al. 2006; Perna et al. 2014). The parent association has a metallicity  $Z = 0.01 \simeq Z_{\odot}$  (based on asteroseismology from Murphy et al. 2021), and mass estimates for  $\zeta$  Oph range from  $13 - 25 M_{\odot}$ , at the lower end of the range where efficient mixing might bring He and CNO-processed material to the surface (chemically homogeneous evolution).

Given the challenges in explaining the surface composition of  $\zeta$  Oph with rotational mixing from the stellar interior and the strong evidence for its past as a member of a binary system, this star offers a unique opportunity to constrain the evolution of accreting stars in massive binary systems.

Here, we present self-consistent binary evolution models for  $\zeta$  Oph computing simultaneously the coupled evolution of *both* donor and accretor star and their orbit. ■ [fix order description] ■ After presenting our calculations in Sec. 2, we show our best model which reproduces the majority of the salient features of this star in Sec. 3. In this model, the surface abundances of  $\zeta$  Oph are explained by pollution from the former companion, rather than upward mixing from the interior of  $\zeta$  Oph itself. We discuss the sensitivity of our results to the admittedly many free parameters required for this kind of computations in Sec. 4. Finally, we conclude in Sec. 6.

## 2. MESA MODELING OF MASSIVE BINARIES

Modeling the evolution of massive binaries ( $M_1 \gtrsim 20 M_{\odot} \geq M_2$ ) is challenging because of the intricate role of several notoriously difficult stellar physics ingredients (differential rotation, mixing, high mass-loss rates, accretion, etc.). Here we follow self-consistently the coupled evolution of two massive stars in a binary system using MESA (version 15140). Our choice of input parameters and our numerical results are available at ■ [link] ■. We discuss here only the main relevant physical parameters, and Appendix A gives more details on our choice of input physics.

We adopt the Ledoux criterion to determine convective stability and a mixing length parameter of 1.5. We include semiconvection and thermohaline mixing follow-

<sup>1</sup> also known as HD 149 757.

<sup>2</sup> The renormalized unit weighted error (RUWE) of this star in *Gaia* EDR3 is 4.48.

ing Langer et al. (1983) and Kippenhahn et al. (1980), respectively, each with efficiency 1.0. We use the exponential core overshooting from Herwig (2000) with free parameters  $(f, f_0) = (4.25 \times 10^{-2}, 10^{-3})$  (Claret & Torres 2017) which broadly reproduce the width of the main sequence from Brott et al. (2011). We also use the local implicit enhancement of the convective flux in superadiabatic regions (MLT--) introduced in MESA 15140.

We treat rotation in the “shellular” approximation and initialize it assuming tidal synchronization at the beginning of the evolution. For our fiducial period choice ( $P = 100$  days), this effectively means both the stars in our binary are initially slow rotators. Our models include in a diffusive approximation the effect of Eddington-Sweet circulations (Sweet 1950), which dominates the chemical mixing due to rotation. We also include the secular and dynamical shear instabilities, and the Goldreich-Schubert-Fricke instability as in Götberg et al. (2017, 2018); Laplace et al. (2020, 2021). We assume a Spruit-Tayler dynamo for the transport of angular momentum (Spruit 2002), and chose the same free parameters as Heger et al. (2000). This also includes the rotational enhancement of wind mass loss as in Langer (1998).

We treat wind mass loss with the Vink et al. (2000, 2001) hot wind, and de Jager et al. (1988) with a scaling factor of 1. This effectively means our wind mass loss rate post-mass transfer is overestimated by almost a factor of 100 (weak wind problem, see Marcolino et al. 2009).

Both stars are evolved simultaneously on the same timesteps until after the donor detaches from its Roche lobe. We follow Kolb & Ritter (1990) to calculate the mass transfer rate from optically thick layers of the donor star during Roche lobe overflow (RLOF). Moreover, we assume that the transferred layers reach the accretor with the accretor’s specific surface angular momentum and entropy, but the chemical composition is determined by the inner evolution of the donor star. Mass transfer is conservative until the accretor reaches critical rotation, after which rotationally enhanced mass loss governs the accretion efficiency.

To define RLOF detachment, we take advantage of the fact that we focus here on case B interactions among massive stars. After losing its envelope, massive donors are not expected to expand to hundreds of  $R_\odot$  during He shell burning at the metallicity we consider (e.g., Laplace et al. 2020). Thus, we define RLOF detachment as the moment after the onset of RLOF when the donor has a surface He mass fraction larger than 0.35 (indicating that a significant amount of envelope has been lost or transferred), a radius smaller than its terminal-age main

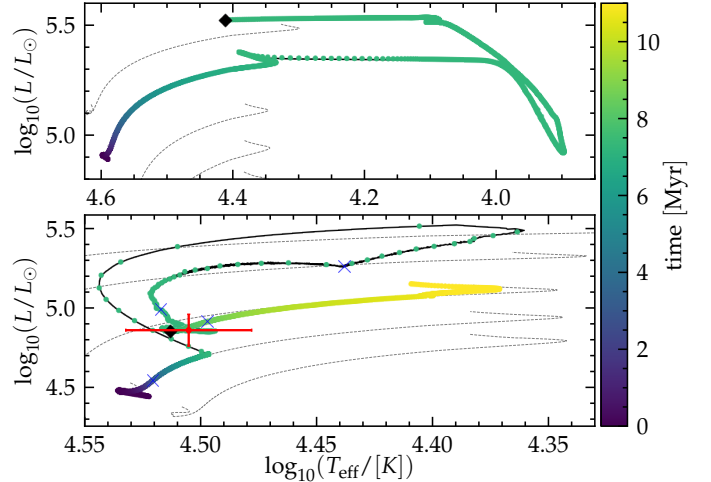


**Figure 1.** HRD for the donor star (top) and accretor star (bottom) of the progenitor binary of  $\zeta$  Oph. Each point is separated by 50 years of evolution. The colors represent the stellar age, the red datapoint shows the position of  $\zeta$  Oph according to VH05, thin blue crosses mark the position of the profiles shown in Fig. 3, and the black diamonds mark the position at the end of the binary run. We continue the accretor evolution as a single star from there until core H depletion, hence the bottom panel shows a longer time. We emphasize the different scales on the two panels. The thin gray dashed line show the main sequence evolution of non-rotating single stars of 15, 17, 25, and 30  $M_\odot$  at  $Z = 0.01$  for comparison.

sequence (TAMS, defined as when the central mass fraction of H drops below  $10^4$ ) radius, and no mass is being transferred anymore. At this point in time, we save a model for the accreting star, and continue its evolution as a single star until TAMS with the same setup.

■ [describe parameter variations in this sec.] ■

### 3. MASSIVE BINARY EVOLUTION NATURALLY EXPLAINS $\zeta$ OPHIUCHI’S PROPERTIES

We describe here the evolution of a binary system where the accretor star can broadly reproduce all the observed features of  $\zeta$  Oph. We assume initial masses  $M_1 = 25 M_\odot$ ,  $M_2 = 17 M_\odot$  on a period of 100 days at  $Z = 0.01$ .

Fig. 1 shows the Hertzsprung-Russell diagrams (HRD) of both stars. After  $\sim 7.24$  Myr, the donor star (top panel) evolves off the main sequence and  $\sim 8400$  years later, when the donor’s effective temperature reaches about  $T_{\text{eff}} \simeq 10^4$  K, mass transfer starts. This results in a stable case B RLOF. We refer to Götberg et al. (2017); Laplace et al. (2021); Blagorodnova et al. (2021) and references therein for a detailed description of the evolution of massive donor stars in binaries. Although

our models are more massive, the qualitative behavior of the donor star is similar.

At the onset of RLOF, the accretor star (bottom panel of Fig. 1) is still on the main sequence with  $T_{\text{eff}} \simeq 10^{4.5}$  K. Because of accretion, it quickly becomes over-luminous ( $L \simeq 10^{5.4} L_{\odot}$ ), and its radius increases dramatically from  $\sim 7.5 R_{\odot}$  to  $\sim 35 R_{\odot}$ . Once the accretor reaches critical rotation (roughly at the lowest  $T_{\text{eff}}$  in the bottom panel of Fig. 1), the star begins contracting and its  $T_{\text{eff}}$  increases. At  $T_{\text{eff}} \simeq 4.43$  K the material transferred from the companion star becomes progressively more He-rich, causing a “v-shaped” feature in the evolutionary track. This indicates that the partially processed outer layers of the donor’s core are uncovered by mass transfer. This late mass transfer puts material at high mean molecular weight  $\mu$  on top of the primordial envelope of the accretor, modifying the morphology of the evolutionary track. Thermohaline mixing starts in the outer layers of the accreting star, and, together with rotational mixing, it progressively dilutes the surface He and N mass fractions and causes noisy features on the HR diagram (e.g., Cantiello et al. 2007). Sec. 3.1 describes in more detail the mixing processes inside the accretor, we emphasize here that the algorithmic choices made to model mixing (and rotation) might impact the morphology of the accretor’s evolutionary track during RLOF. However, the entire duration of RLOF (and thus of the feature in the bottom panel of Fig. 1 from the departure from the main-sequence to the black diamond) is only about  $10^4$  years.

We evolve the binary system until the black diamonds in Fig. 1, which occurs well after the donor detaches from the Roche Lobe. At this point, the accretor is a H-rich fast-rotating star of  $\sim 20.1 M_{\odot}$ . Available mass estimates for the presently single  $\zeta$  Oph are highly uncertain, but most include  $20 M_{\odot}$  (e.g., Hoogerwerf et al. 2001, VH05, Neuhäuser et al. 2020). The accretor’s post-RLOF orbital velocity is  $v_2 \simeq 40 \text{ km s}^{-1}$ , which is expected to decrease a bit further due to wind-driven widening of the binary, but is in good agreement with the presently observed runaway velocity of  $\zeta$  Oph.

Accounting for both wind mass loss and the amount of mass transferred, at the end of RLOF the donor becomes a He star of  $\sim 9.4 M_{\odot}$ , likely to contract further and appear as a Wolf-Rayet star. Its surface H mass fraction is  $\lesssim 0.2$  and most of the H is likely to be removed by further wind mass loss (e.g., Göteborg et al. 2017).

■ [Ylva: want to expand?] ■. ■ [maybe move next paragraph to discussion?] ■ For our assumed scenario to work, such donor needs to successfully explode in a SN, breaking the binary system and making a neutron star remnant. While the post-

RLOF donor mass we obtain is rather high, recent studies suggest higher “explodability” of donor stars in binary systems (e.g., Schneider et al. 2021; Laplace et al. 2021; ?). Furthermore, neither the initial donor mass  $M_1$  nor the initial period are observable, and thus there is room to chose different values to obtain easier to explode donors and faster (or slower) accretors post-RLOF.

From the black diamond onwards, we evolve the accretor as a single star with the same MESA setup until TAMS. The main-sequence track on which the accretor settles post-RLOF has a higher luminosity compared to the original track because of the accretion of mass, and it has also a slightly different slope due to the close-to-critical rotation and the accretion of partially nuclearly processed material (He- and N-rich) material.

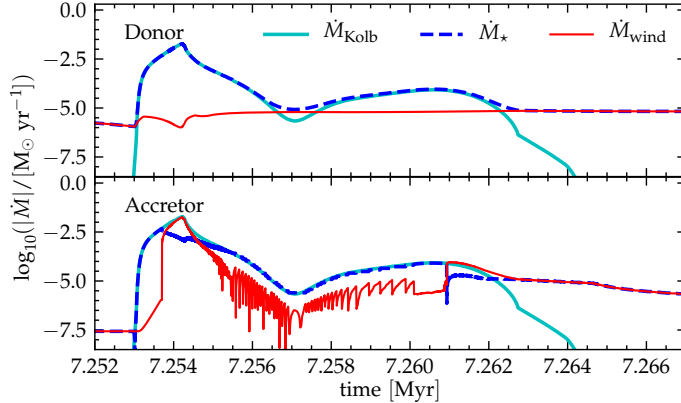
The red errorbars in the bottom panel of Fig. 1 mark the approximate position of  $\zeta$  Oph based on the analysis of VH05. The color of the track in Fig. 1 indicate that our accreting star spends about  $\sim 2$  Myr within the represented errorbars after the end of RLOF. Assuming the kinematic age of  $1.78 \pm 0.21$  (Neuhäuser et al. 2020), and estimating a remaining lifetime of the donor of  $\sim 0.5$  Myr, this gives the correct timescale for the binary SN scenario. The observed position of  $\zeta$  Oph on the HRD, and especially its relatively high  $T_{\text{eff}}$  would be hard to reproduce assuming initially less massive accretors (which would remain too cool even after accreting mass), or more equal initial mass ratio (which would produce a too evolved accretor at the onset of mass transfer).

Fig. 2 shows the rate of mass change for each star during RLOF. The top panel focuses on the donor star which loses mass to RLOF (cyan line) and wind mass loss (thin red line). The dashed blue lines show their combination resulting in the actual rate of mass change of the stars. The bottom panel shows instead the accreting star, which grows in mass because of the mass transfer. At peak the mass transfer rates reaches very high values above  $10^{-2.5} M_{\odot} \text{ yr}^{-1}$ , and taps into the optically thick matter of the donor.

During RLOF, the total amount of mass lost by the donor is  $\Delta M_{\text{donor}} \simeq 10.6 M_{\odot}$ , of which only  $\Delta M_{\text{accretor}} \simeq 3.4 M_{\odot}$  are successfully accreted. This corresponds to an overall mass transfer efficiency  $\beta_{\text{RLOF}} \equiv \Delta M_{\text{accretor}} / \Delta M_{\text{donor}} \simeq 0.3$ , although the accretion efficiency is *not* constant throughout the mass transfer (e.g., van Rensbergen et al. 2006), instead it depends on the radial and rotational evolution of the accreting star.

At the end of RLOF, the donor star briefly expands again ( $T_{\text{eff}} \simeq 10^{4.1}$  K,  $L \simeq 10^{5.5} L_{\odot}$ ). This is due to the





**Figure 2.** Mass transfer rates as a function of time during RLOF. The top (bottom) panel shows the donor (accretor) star. The cyan solid lines show the mass transfer rate between the two stars. The dashed blue lines show the actual change in the mass of the stars (due to the combination of wind, and accretion efficiency). The thin red lines show the wind mass loss rates. During RLOF the accretor reaches critical rotation, which leads to oscillations in the rotationally-enhanced wind mass loss.

partial recombination of the now He-rich outer layers, which causes a transient surface convection layer. This causes the second broad peak in the mass transfer rates centered at 7.261 Myrs. We find this to be the culprit of difficulties in modeling massive binaries transferring mass in older MESA releases, because although only a very small amount of mass is involved, this would lead to large radial expansion much beyond the donor’s Roche lobe, and cause numerical problems.

The wind mass loss (in red) controls the accretion efficiency and thus the difference between the actual rate of change in mass of the accretor (thick dashed blue) and the rate at which mass is being transferred. At peak, where the red and the cyan lines overlap, mass transfer becomes very non-conservative, but for most of the evolution the (rotationally enhanced) wind removes only a fraction of the accreted mass. The interplay between the stellar radius and rotation causes the oscillations visible in the bottom panel, whose amplitude is generally lower than the RLOF mass transfer rate.

### 3.1. Mixing and composition

MESA treats mixing processes in the diffusion approximation (Paxton et al. 2011). To illustrate the dominant processes throughout the accretor’s evolution, we show in Fig. 3 the diffusion coefficients for various mixing processes as a function of mass coordinate at selected times. Each panel corresponds to one of the thin blue crosses in the bottom panel of Fig. 1, and the gray shaded areas mark mass accreted during RLOF. The last panel

roughly represents the predicted internal structure of  $\zeta$  Oph as observed today.

In Fig. 3, the thin red lines correspond to convection, with the initial convective core of  $\sim 6 M_{\odot}$  clearly visible in the first panel. In all models, a tiny sub-surface convective region is also visible in the outermost layers (see e.g., Cantiello et al. 2021). The thin blue lines mark mixing processes that are not related to rotation, nor are any of the other processes explicitly shown, which here effectively means overshooting. The extension of the diffusion coefficient above the convective core in all panels is the typical behavior for an exponentially decreasing overshooting. Purple and pink represent semi-convection and thermohaline mixing, respectively. Before mass transfer (left-most panel), only a small amount of sub-surface thermohaline mixing occurs, with a mass extent comparable or smaller to the sub-surface convective zone, and no semiconvection occurs. The thick cyan line corresponds to the total diffusion coefficient, obtained as the sum of the diffusion coefficients for each process modeled: where the cyan line is not overlapping with the others, rotational mixing (and more specifically Eddington-Sweet meridional circulation) is the dominant process.

During RLOF (second and third panel), the spin-up due to accretion causes an increase in the rotational mixing (see also Sec. 3.2), and the accretion of nuclearly processed material progressively widens the thermohaline mixing region at the surface. Late during the mass transfer (third panel), thermohaline mixing dominates the outermost layers – except within the sub-surface convective zone, but throughout most of the envelope rotation does the lion’s share of the mixing. Thermohaline mixing and Eddington-Sweet circulations together mix inwards and dilute the CNO-enriched material coming from the donor’s surface.

At the same time, the increase in the accretor mass drives rejuvenation (e.g., Schneider et al. 2016). This can be seen as a growth of the convective core from  $\sim 6 M_{\odot}$  to almost  $\sim 8 M_{\odot}$ , plus the corresponding growth of the overshooting region. This mixes inward H-rich material resulting in an elongation of the accretor’s lifetime, and at the same time mixes outward CNO-equilibrium matter, connecting the N-rich core with the outer envelope polluted from the top.

Tab. 1 summarizes the surface properties of the accretor star at the time shown in the last panel of Fig. 3, that is shortly after the RLOF phase, while the model is still roughly at the observed position of  $\zeta$  Oph.

Both the mass and radius agree reasonably well with the estimates from VH05 and previous studies, that is  $20 M_{\odot}$  and  $8.3 \pm 1.5 R_{\odot}$ , respectively. The surface

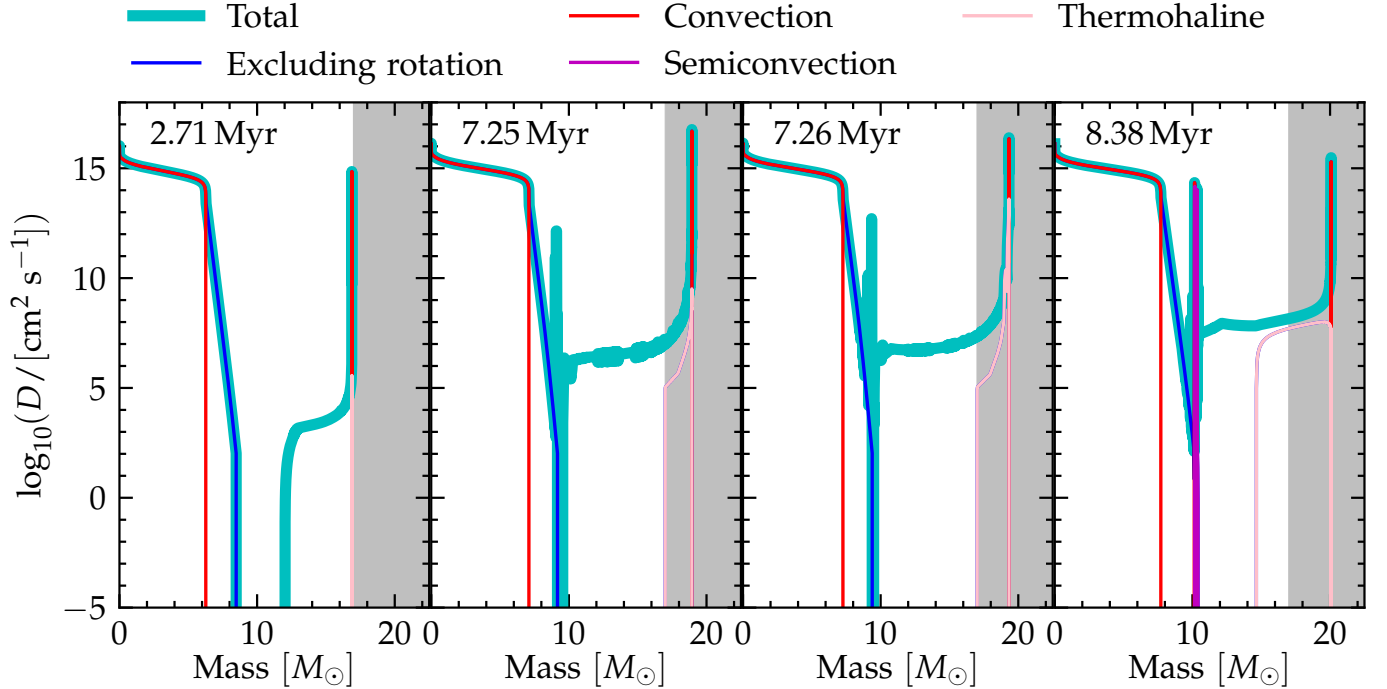


**Figure 3.** Mixing diffusion coefficients in the accretor star. From left to right, each panel shows times during the main sequence (2.71 Myr), right before the “v-shaped” feature during RLOF (7.25 Myr), close to the end of RLOF (7.26 Myr), and after mass transfer (8.38 Myr) – see the corresponding thin blue crosses in Fig. 1. The total diffusion coefficient (thick cyan line) is obtained as the sum of non-rotational mixing processes (i.e., here overshooting, thin blue line), convection (shown in red), thermohaline mixing (pink) and semiconvection (in purple). The gray area corresponds to mass accreted during RLOF.

$M [M_{\odot}]$	$R [R_{\odot}]$	$\log_{10}(\omega/[s^{-1}])$	$v_{\text{rot}} [\text{km s}^{-1}]$	$X(^1\text{H})$	$X(^4\text{He})$	$X(^{12}\text{C})$	$X(^{14}\text{N})$	$X(^{16}\text{O})$
20.1	9.6	-4.263	366.1	0.678010	0.312093	0.001344	0.001340	0.004148

**Table 1.** Properties of the accretors shortly after the end of RLOF (last thin blue cross in Fig. 1 and last panel of Fig. 3).

rotational velocity in excess of  $350 \text{ km s}^{-1}$  is also in the correct ballpark albeit possibly on the low end. We report the surface H mass fraction<sup>3</sup>, lower than primordial because of the accretion of nuclearily processed material, and the surface mass fraction of the most prominent species  $^4\text{He}$ ,  $^{12}\text{C}$ ,  $^{14}\text{N}$ ,  $^{16}\text{O}$ . Assuming our surface H mass fraction  $X(^1\text{H})$ , the corresponding mass fractions of  $^4\text{He}$ ,  $^{12}\text{C}$ ,  $^{14}\text{N}$ ,  $^{16}\text{O}$  obtained by [VH05](#) are  $0.33^{+0.14}_{-0.05}$ ,  $0.0006 \pm 0.0004$ ,  $0.002 \pm 0.001$ , and  $0.005 \pm 0.004$ . Our values are sensitive to the interplay between several poorly understood processes treated in one dimension: mass accretion efficiency, rotationally enhanced wind mass loss, thermohaline, and inward rotational mixing. Therefore, although not perfect, we consider the match with the mass fractions reported by [VH05](#) surprisingly satisfactory.

<sup>3</sup> This is needed to convert mass fractions reported here into  $\varepsilon(X) = 12 + \log_{10}(N_X/N_H)$ , where  $N_X$  and  $N_H$  are the number fractions of species  $X$  and H, respectively.

### 3.1.1. Comparison to single fast-rotating stars

We now compare the mixing processes happening in a single rotating massive stars and in our accretor model. Fig. 4 shows the mass fraction of  $^{14}\text{N}$  as a function of mass coordinate along the evolution of three  $20 M_{\odot}$  stars initialized with  $\omega/\omega_{\text{crit}} = 0.2, 0.3, 0.4, 0.5$  where  $\omega$  is the surface angular frequency and  $\omega_{\text{crit}} = \sqrt{(1 - L/L_{\text{Edd}})GM/R^3}$  and  $L_{\text{Edd}}$  is the Eddington luminosity computed using the stellar opacity from the outermost mesh point down to optical depth  $\tau = 2/3$ ,  $L$  is the luminosity,  $R$  the radius of the star, and  $G$  the gravitational constant. These rotating single stars have an otherwise identical setup as our binary model. The last panel of Fig. 4 shows our accretor model. The dotted red line marks the primordial mass fraction of  $^{14}\text{N}$  for the adopted  $Z = 0.01$ , the thin dashed lines mark the surface value at TAMS.

The colored tracks show selected profiles throughout the main sequence, with lighter colors corresponding to more evolved stars. The accretor model (rightmost

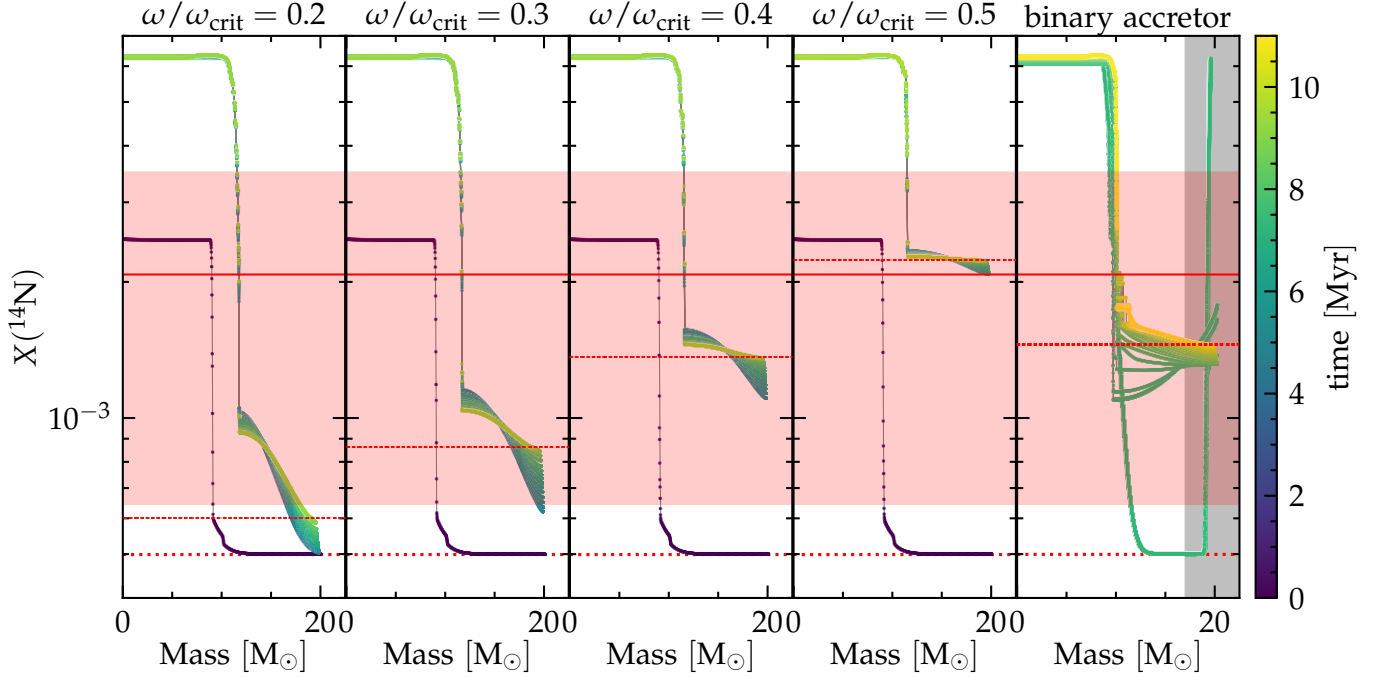


**Figure 4.**  $^{14}\text{N}$  mass fraction as a function of mass coordinate for  $20 M_{\odot}$  single star models with increasing  $\omega/\omega_{\text{crit}}$  at birth (first four panels), and for the accretor of our fiducial binary. The dotted thick red line marks the primordial value, the thin dashed red line marks the surface value at TAMS. In the last panel, the gray area highlights mass accreted during RLOF. The colors of each profile go from dark to light at TAMS, and selected profiles along the main sequence are shown. The solid red line and the shaded red region correspond to the mass fraction of  $^{14}\text{N}$  estimated by V05 assuming the surface mass fraction of H from Tab. 1. The abundance of  $^{14}\text{N}$  alone is not strongly constraining.

panel) starts as a  $17 M_{\odot}$  and is rejuvenated by binary interactions, thus it reaches TAMS at 11.24 Myr. For comparison, the initially  $20 M_{\odot}$  rotating models have a main-sequence lifetime of 9.2–9.6 Myr (longer for higher initial rotation rates), hence their TAMS profile does not have as light a color in Fig. 4.

The first four panels of Fig. 4 show the typical rotational mixing profiles:  $^{14}\text{N}$  rapidly rises in the core because of the CNO burning, and it is then mixed outwards. At any time the  $^{14}\text{N}$  profile is monotonically decreasing in mass coordinate, and the higher the initial rotation, the higher the surface  $^{14}\text{N}$  mass fraction reached at TAMS.

Conversely, the  $^{14}\text{N}$  mass fraction profile of the accretor is *not* monotonic throughout the evolution. It is shaped not only by outward rotational mixing, but also by the accretion of matter from the outer layers of the donor’s star core mixed inward by rotation and thermohaline mixing.

Initially, the tidally synced accretor star rotates too slowly for significant outward rotational mixing out of the core, and until the onset of RLOF (roughly at 7.25 Myr) no appreciable variation of the surface  $X(^{14}\text{N})$  occurs. During late RLOF after the “v-shaped” feature in Fig. 1, N-rich material from the donor’s core piles

onto the accretor’s surface – inside the gray area in the rightmost panel of Fig. 4. The close-to-critical rotation of the accretor and the inversion in the mean molecular weight  $\mu$  then drive inward mixing (see also Fig. 3) of this N-rich material and dilute it in the envelope.

Simultaneously, the mere growth in mass causes the steepening of the core-temperature gradient and increase in the convective core mass (rejuvenation, e.g., Schneider et al. 2016), driving some outward convective mixing of N-rich material. Because convection turnover timescales are much shorter than evolutionary timescales, the growth of the convective core produces “steps” at the outer edge of the core (slightly outside mass coordinate  $10 M_{\odot}$ ). In the post-RLOF evolution, outward rotational mixing from the rejuvenated core and inward rotational mixing and thermohaline mixing from the surface connect the excess  $^{14}\text{N}$ .

In Fig. 4, the solid red line and red shaded area across all panels show the  $^{14}\text{N}$  from V05 (assuming the surface mass fraction from our model listed in Tab. 1): the mass fraction of  $^{14}\text{N}$  alone is not sufficient to distinguish with these models, and already a moderate  $\omega/\omega_{\text{crit}} \geq 0.3$  is sufficient for models to reach the lower-limit of the error bar.

### 3.2. Angular momentum transport and surface rotation

One of the main distinguishing features of  $\zeta$  Oph is its extremely high surface rotation rate. Spectroscopic measurements of the projected rotational velocity exceed  $v \sin(i) \gtrsim 400 \text{ km s}^{-1}$ , which implies close to critical rotation. Zehe et al. (2018) recently estimated  $v \sin(i) = 432 \pm 16 \text{ km s}^{-1}$  and  $i \sim 56$  degrees.

Fig. 5 shows the surface average rotation rate of our accretor model as a function of time (ignoring the projection angle  $i$ ). The dark red band corresponds to the  $v \sin(i)$  from Zehe et al. (2018), and the lighter band shows a range of 5 times their error bar.

The initial binary is wide enough that the initial tidal synchronization implies a very low rotation. At 7.25 Myr, RLOF rapidly spins up the accretor to critical rotation, up to  $v_{\text{crit}} \simeq 520 \text{ km s}^{-1}$ . The star remains fast rotating throughout the mass transfer phase, which ends at the black diamond in Fig. 5. In the remaining evolution, the star spins down progressively through wind mass loss, and within  $\sim 2$  Myr its averaged surface rotational velocity drops below  $350 \text{ km s}^{-1}$ . Close to the end of the main sequence, the internal transport of angular momentum causes a change in the spin-down slope.

Fig. 5 shows that, without accounting for the inclination angle, our model can retain a significant surface rotation for a time comparable to the kinematic age of the star, which is shorter than the remaining main-sequence lifetime. We emphasize that throughout its evolution this model is computed using the Vink et al. (2000, 2001) wind mass-loss rate with full efficiency. Marcolino et al. (2009) found the predicted mass loss rate to exceed the observed one by  $\sim 2$  orders of magnitude. While this could impact the evolution of the binary even before RLOF, it certainly increases the spin-down rate of our model compared to the observations. We attempted running models with artificially decreased wind mass loss rate (e.g., Renzo et al. 2017), but these resulted in super-critical  $\omega/\omega_{\text{crit}} > 1$  accretor stars with untrustworthy numerical results. Nevertheless, we expect that an accreting star modeled with lower wind-mass loss rate post-RLOF would retain an even higher surface rotation for longer.

#### 3.2.1. Comparison to single fast-rotating stars

To illustrate the angular momentum transport in our accretor stars, it is helpful to compare with the single rotating  $20 M_{\odot}$  models. The internal rotational profile of a single star rigidly rotating at birth is different than the profile obtained spinning up the secondary star at a later evolutionary stage and from its surface. This even

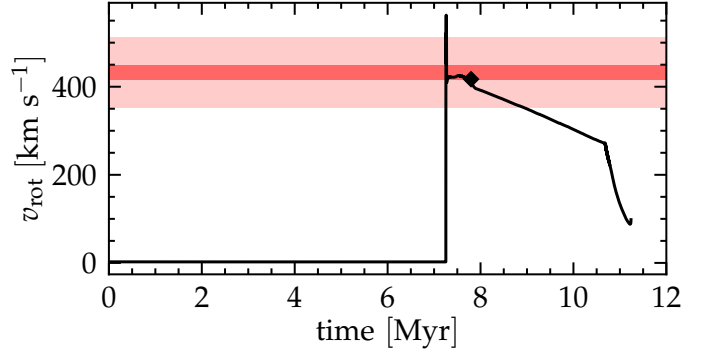


**Figure 5.** Surface averaged rotation rate for the accretor model. At  $\sim 7.25$  Myr the mass transfer quickly spins up the accretor at critical rotation. By the time the donor detaches from the RLOF the accretor is still spinning at  $\sim 400 \text{ km s}^{-1}$ . At this point (beginning of the dot-dashed line), we continue the evolution as a single star, and the accretor quickly spins down. Note however that we use a wind mass-loss rate from Vink et al. (2001), which is observed to be  $\sim 2$  orders of magnitude too high (Marcolino et al. 2009).

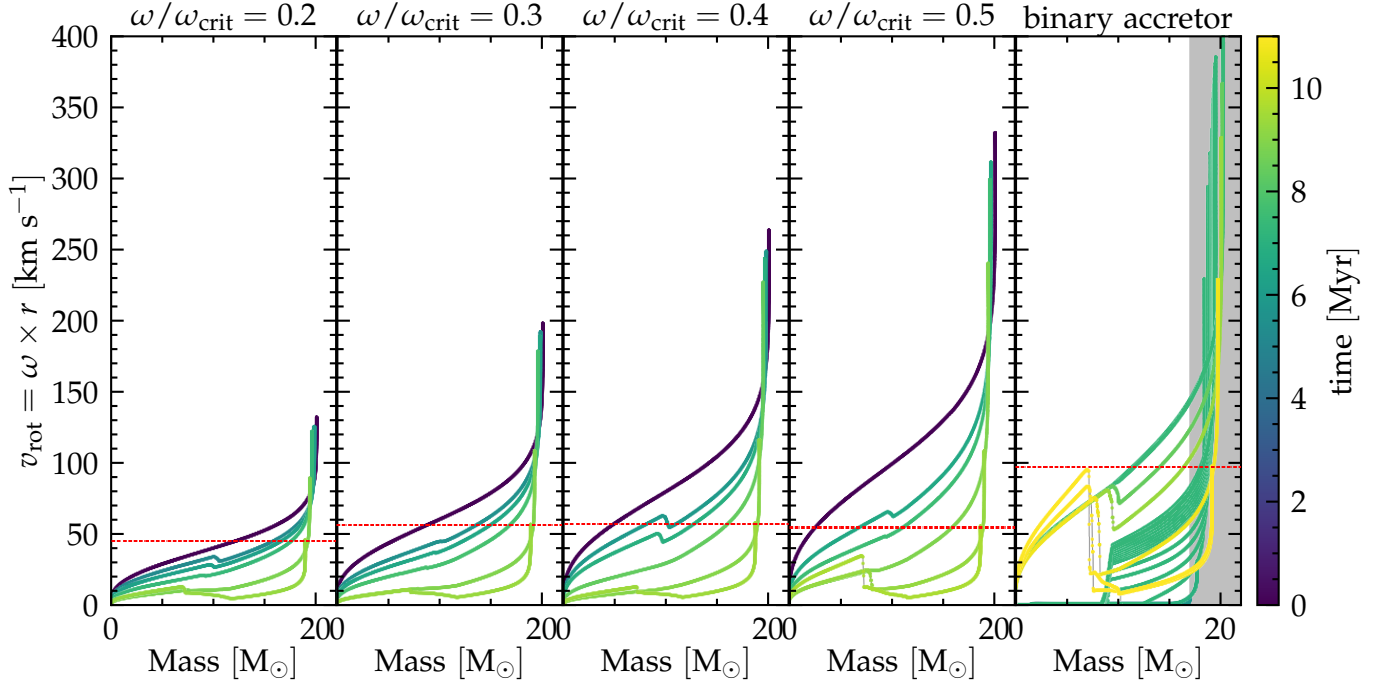
within the framework of a specific model for the angular momentum transport in stars (Spruit 2002).

Fig. 6 shows the internal equatorial rotational velocity  $v_{\text{rot}} = \omega \times r$ . As in Fig. 4, the first four panels show single rotating stars with increasing initial  $\omega/\omega_{\text{crit}}$ , the last panel shows our accretor model, and the colors go from dark (close to zero age main sequence, ZAMS) to light (TAMS), with the accretor reaching lighter colors because of its rejuvenation. The gray area in the last panel represents mass accreted during RLOF.

The thin dashed red lines in each panel mark the TAMS surface rotation rates: all our single star models reach a TAMS surface  $v_{\text{rot}} \simeq 50 \text{ km s}^{-1}$ . Initially faster rotating models spin down more in their outer layers, have slightly longer main sequence lifetimes (because of rotational mixing increasing the available fuel), and develop stronger differential rotation which drives more inwards transport of angular momentum. The single star profiles show the progressive development of a core-envelope interface, and the core rotation rate is sensitive to the initial value of  $\omega/\omega_{\text{crit}}$ .

Conversely, the last panel shows that the entire interior of the accretor has a negligible equatorial rotational velocity until RLOF. Because of binary interactions, rotation does not start as rigid, but instead angular momentum is injected from the top. In our model, inward transport of angular momentum creates the monotonically increasing  $v_{\text{rot}}$  profile seen in the green lines of the last panel. When angular momentum is transported across the chemical gradient at the edge of the convective core, a discontinuity stronger than in the single stars arises.





**Figure 6.** Internal rotational profile for  $20 M_{\odot}$  single star models with increasing  $\omega/\omega_{\text{crit}}$  at birth (first four panels), and for the accretor of our fiducial binary. As in Fig. 4, the colors go from dark (close to ZAMS) to light at TAMS, and the thin dashed red line mark the TAMS surface rotation rate. In the last panel, the gray area indicates mass accreted during RLOF. The yellow lines (TAMS) in the last panel show that the core of the accretor is rotating almost as fast as its surface, and both are faster than the surface of single star models.

By the end of the main-sequence evolution of the accretor, the surface still spins with  $v_{\text{rot}} \simeq 100 \text{ km s}^{-1}$  (twice as fast as the single star models). Perhaps more importantly, the outer-edge of the core has a similar rotational velocity as the surface, and much larger than the rotational velocity of the single star models. This might have important implications for the rotation rate of the compact objects formed by the initially less massive star in a binary, and the models of compact objects spins for gravitational-wave progenitors (e.g., Zaldarriaga et al. 2018; Qin et al. 2018; Callister et al. 2020).

#### 4. ROBUSTNESS OF THE MODEL

In this section we investigate the sensitivity of our results to physical parameters.

■ [How to present results? Table? Showing what? surface mass fractions, rotation, L, Teff] ■

■ [ Binary parameters:

- $M_1$
- $M_2$
- $P$
- J-accretion

] ■

■ [ Single star parameters:

- thermohaline mixing
- Eddington-Sweet circulations
- metallicity

] ■

■ [others?] ■

#### 5. DISCUSSION

##### 5.1. Free parameters in the treatment of mass transfer

We regulate the accretion efficiency through the rotational enhancement of mass loss (e.g. Langer 1998).

■ [maybe move  $\beta_{\text{RLOF}}$  here] ■. However, (??) argued that accretion of mass (but no angular momentum) might be possible even at critical rotation.

##### 5.2. The explosion of the former companion

Throughout this study, we have assumed the “binary SN scenario”: after the mass transfer phase, the explosion of the donor breaks the binary and ejects the accretor with roughly its pre-explosion velocity (e.g., Renzo et al. 2019). This is the fate of the majority of massive

binary systems, and  $\zeta$  Oph might be the best example of this scenario (e.g., [Blaauw 1952, 1961](#); [Hoogerwerf et al. 2000](#)). [Neuhäuser et al. \(2020\)](#) suggested not only the companion successfully exploded producing the pulsar PSR B1706-16, but that the explosion produced radioactive  $^{60}\text{Fe}$  which polluted Earth. From kinematic and orbital considerations they estimated a natal kick of  $\sim 250 \text{ km s}^{-1}$ , which would be sufficiently large to unbind the binary. ■ **[check, be more precise]** ■

However, we have so far neglected the impact of the explosion on the structure of the accretor star. The blast wave will hit the companion at a ■ **[estimate solid angle]** ■ causing mass loss – directly via ablation and by injecting energy in the envelope, inflating it and enhancing its wind ([Wheeler et al. 1975](#); [Tauris & Takens 1998](#); [Podsiadlowski 2003](#); [Hirai et al. 2018](#)).

Using 2D hydrodynamic simulations of the star-SN ejecta interactions in close binaries ( $a \lesssim 60 R_{\odot}$ , cf.  $a \gtrsim 343 R_{\odot}$  in our fiducial binary model), [Hirai et al. \(2018\)](#) found that the companion star recovers its pre-explosion luminosity and effective temperature within a few years to decades, and the amount of mass removed by the SN shock is  $\lesssim 10^{-2} M_{\odot}$

■ **[estimate mass loss]** ■

Because of the SN shock, the just ejected new runaway star might appear bloated and redder (long before it overtakes the slowing SN remnant). Hydrodynamical simulations of a non-rotating star with a SN shock suggest that within ■ **[X]** ■ the star returns in equilibrium [Hirai et al. \(2018\)](#). The impact of this brief out of thermal equilibrium phase on the stellar spin should be investigated further.

The SN ejecta might also pollute the surface of the runaway depositing processed nuclear material (e.g. [Przybilla et al. 2008](#)). However, enhanced mass loss, and rapid rotating might rapidly dilute the yields.

■ **[improve this sec.]** ■

#### A. MESA SETUP

■ **[MLT-?]** ■

■ **[possibly move to methods]** ■ We use MESA version 15140 to compute our models. The MESA equation of state (EOS) is a blend of the OPAL [Rogers & Nayfonov \(2002\)](#), SCVH [Saumon et al. \(1995\)](#), PTEH [Pols et al. \(1995\)](#), HELM [Timmes & Swesty \(2000\)](#), and PC [Potekhin & Chabrier \(2010\)](#) EOSes. ■ **[check if updated EOS?]** ■

Radiative opacities are primarily from OPAL ([Iglesias & Rogers 1993, 1996](#)), with low-temperature data

On top of the surface abundances, its extreme rotation rate, and the peculiar space velocity,  $\zeta$  Oph poses a number of other puzzles: its wind mass-loss rate is about two orders of magnitude lower than theoretical predictions (weak wind problem, [Marcolino et al. 2009](#)), the star exhibits spectral variability with occasional appearance of  $\text{H}\alpha$  in emission (e.g., [Walker et al. 1979](#)).

#### 6. CONCLUSIONS

We have demonstrated that self-consistent one-dimensional calculations of coupled stellar models with masses  $\gtrsim 20 M_{\odot}$  are possible with the MESA software instrument. As a first application, we focused on finding a model for  $\zeta$  Oph, assuming its runaway nature is explained by the binary SN scenario.

We found that it is likely possible to explain its surface composition without assuming that the surface excess of He and N comes from within the star. Instead, this material comes from the receding core of the donor star. Therefore, the present day abundances constrain the accretion efficiency and mixing in the accretor.

$\zeta$  Oph should therefore *not* be used to test models of rotational mixing in single star evolution, nor its more extreme version of chemically homogeneous evolution.

*Software:* `mesaPlot` ([Farmer 2018](#)), `mesaSDK` ([Townsend 2018](#)), `ipython/jupyter` ([Pérez & Granger 2007](#)), `matplotlib` ([Hunter 2007](#)), `NumPy` ([van der Walt et al. 2011](#)), `MESA` ([Paxton et al. 2011, 2013, 2015, 2018, 2019](#))

#### ACKNOWLEDGMENTS

We are grateful to E. Zapartas, A. Jermyn, M. Cantiello for helpful discussions.

#### APPENDIX

from [Ferguson et al. \(2005\)](#) and the high-temperature, Compton-scattering dominated regime by [Buchler & Yueh \(1976\)](#). Electron conduction opacities are from [Cassisi et al. \(2007\)](#).

Nuclear reaction rates are a combination of rates from NACRE ([Angulo et al. 1999](#)), JINA REACLIB ([Cyburt et al. 2010](#)), plus additional tabulated weak reaction rates [Fuller et al. \(1985\)](#); [Oda et al. \(1994\)](#); [Langanke & Martínez-Pinedo \(2000\)](#). Screening is included via the prescription of [Chugunov et al. \(2007\)](#). Thermal neutrino loss rates are from [Itoh et al. \(1996\)](#). We use a 22-isotope nuclear network (`approx_21_plus_cr56`).

The inlists, processing scripts, and model output will be made available at [link](#).

## B. RESOLUTION TESTS

### B.1. *Spatial resolution*

## REFERENCES

- Almeida, L. A., Sana, H., Taylor, W., et al. 2017, *A&A*, 598, A84, doi: [10.1051/0004-6361/201629844](#)
- Angulo, C., Arnould, M., Rayet, M., et al. 1999, *Nuclear Physics A*, 656, 3, doi: [10.1016/S0375-9474\(99\)00030-5](#)
- Belczynski, K., Holz, D. E., Bulik, T., & O’Shaughnessy, R. 2016, *Nature*, 534, 512, doi: [10.1038/nature18322](#)
- Blaauw, A. 1952, *BAN*, 11, 414
- . 1961, *BAN*, 15, 265
- Blaauw, A. 1993, in *Astronomical Society of the Pacific Conference Series*, Vol. 35, *Massive Stars: Their Lives in the Interstellar Medium*, ed. J. P. Cassinelli & E. B. Churchwell, 207
- Blagorodnova, N., Klencki, J., Pejcha, O., et al. 2021, arXiv e-prints, arXiv:2102.05662.  
<https://arxiv.org/abs/2102.05662>
- Bodensteiner, J., Baade, D., Greiner, J., & Langer, N. 2018, *A&A*, 618, A110, doi: [10.1051/0004-6361/201832722](#)
- Braun, H., & Langer, N. 1995, *A&A*, 297, 483
- Broekgaarden, F. S., Berger, E., Neijssel, C. J., et al. 2021, arXiv e-prints, arXiv:2103.02608.  
<https://arxiv.org/abs/2103.02608>
- Brott, I., de Mink, S. E., Cantiello, M., et al. 2011, *A&A*, 530, A115, doi: [10.1051/0004-6361/201016113](#)
- Buchler, J. R., & Yueh, W. R. 1976, *ApJ*, 210, 440, doi: [10.1086/154847](#)
- Callister, T. A., Farr, W. M., & Renzo, M. 2020, arXiv e-prints, arXiv:2011.09570.  
<https://arxiv.org/abs/2011.09570>
- Cantiello, M., Lecoanet, D., Jermyn, A. S., & Grassitelli, L. 2021, arXiv e-prints, arXiv:2102.05670.  
<https://arxiv.org/abs/2102.05670>
- Cantiello, M., Yoon, S., Langer, N., & Livio, M. 2007, *A&A*, 465, L29
- Cassisi, S., Potekhin, A. Y., Pietrinferni, A., Catelan, M., & Salaris, M. 2007, *ApJ*, 661, 1094, doi: [10.1086/516819](#)
- Chugunov, A. I., Dewitt, H. E., & Yakovlev, D. G. 2007, *PhRvD*, 76, 025028, doi: [10.1103/PhysRevD.76.025028](#)
- Claret, A., & Torres, G. 2017, *ApJ*, 849, 18, doi: [10.3847/1538-4357/aa8770](#)
- Cyburt, R. H., Amthor, A. M., Ferguson, R., et al. 2010, *ApJS*, 189, 240, doi: [10.1088/0067-0049/189/1/240](#)
- De Donder, E., Vanbeveren, D., & van Bever, J. 1997, *A&A*, 318, 812
- de Jager, C., Nieuwenhuijzen, H., & van der Hucht, K. A. 1988, *A&AS*, 72, 259
- Eldridge, J. J., Langer, N., & Tout, C. A. 2011, *MNRAS*, 414, 3501, doi: [10.1111/j.1365-2966.2011.18650.x](#)
- Evans, F. A., Renzo, M., & Rossi, E. M. 2020, arXiv e-prints, arXiv:2006.00849.  
<https://arxiv.org/abs/2006.00849>
- Farmer, R. 2018, rjfarmer/mesaplot, doi: [10.5281/zenodo.1441329](#)
- Ferguson, J. W., Alexander, D. R., Allard, F., et al. 2005, *ApJ*, 623, 585, doi: [10.1086/428642](#)
- Fuller, G. M., Fowler, W. A., & Newman, M. J. 1985, *ApJ*, 293, 1, doi: [10.1086/163208](#)
- Götberg, Y., de Mink, S. E., & Groh, J. H. 2017.  
<https://arxiv.org/abs/1701.07439>
- Götberg, Y., de Mink, S. E., Groh, J. H., et al. 2018, *A&A*, 615, A78, doi: [10.1051/0004-6361/201732274](#)
- Heger, A., Langer, N., & Woosley, S. E. 2000, *ApJ*, 528, 368
- Hellings, P. 1983, *Ap&SS*, 96, 37, doi: [10.1007/BF00661941](#)
- . 1984, *Ap&SS*, 104, 83, doi: [10.1007/BF00653994](#)
- Herrero, A., Kudritzki, R. P., Vilchez, J. M., et al. 1992, *A&A*, 261, 209
- Herwig, F. 2000, *A&A*, 360, 952
- Hirai, R., Podsiadlowski, P., & Yamada, S. 2018.  
<https://arxiv.org/abs/1803.10808>
- Hoogerwerf, R., de Bruijne, J. H. J., & de Zeeuw, P. T. 2000, *ApJL*, 544, L133, doi: [10.1086/317315](#)
- . 2001, *A&A*, 365, 49, doi: [10.1051/0004-6361:20000014](#)
- Hunter, J. D. 2007, *Computing In Science & Engineering*, 9, 90
- Iglesias, C. A., & Rogers, F. J. 1993, *ApJ*, 412, 752, doi: [10.1086/172958](#)
- . 1996, *ApJ*, 464, 943, doi: [10.1086/177381](#)
- Itoh, N., Hayashi, H., Nishikawa, A., & Kohyama, Y. 1996, *ApJS*, 102, 411, doi: [10.1086/192264](#)
- Kippenhahn, R., Ruschenplatt, G., & Thomas, H.-C. 1980, *A&A*, 91, 175
- Kippenhahn, R., & Weigert, A. 1967, *ZA*, 65, 251
- Klencki, J., Nelemans, G., Istrate, A. G., & Chruslinska, M. 2021, *A&A*, 645, A54, doi: [10.1051/0004-6361/202038707](#)

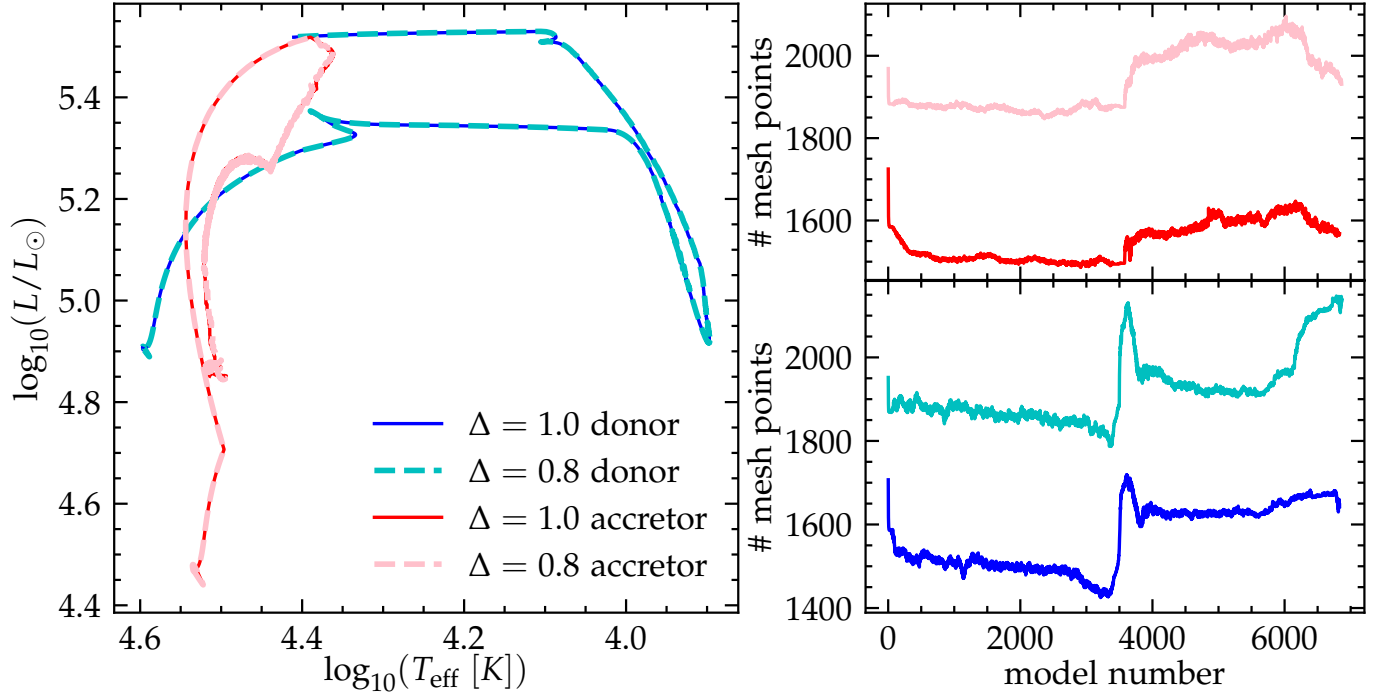


**Figure 7.** Left: HRD comparison for our fiducial binary model varying the number of mesh points. We only show the evolution until our definition of RLOF detachment. Right: number of mesh points as a function of timestep number. In both panels, the blue/cyan tracks show the donor stars, the red/pink tracks show the accretor. Thicker dashed lines correspond to the models at higher resolution (i.e., lower  $\Delta$  which indicates the value of `mesh_delta_coeff`).

- Kolb, U., & Ritter, H. 1990, *A&A*, 236, 385
- Langanke, K., & Martínez-Pinedo, G. 2000, *Nuclear Physics A*, 673, 481, doi: [10.1016/S0375-9474\(00\)00131-7](https://doi.org/10.1016/S0375-9474(00)00131-7)
- Langer, N. 1998, *A&A*, 329, 551
- Langer, N., Fricke, K. J., & Sugimoto, D. 1983, *A&A*, 126, 207
- Laplace, E., Götberg, Y., de Mink, S. E., Justham, S., & Farmer, R. 2020, *A&A*, 637, A6, doi: [10.1051/0004-6361/201937300](https://doi.org/10.1051/0004-6361/201937300)
- Laplace, E., Justham, S., Renzo, M., et al. 2021, *arXiv e-prints*, arXiv:2102.05036, <https://arxiv.org/abs/2102.05036>
- Law-Smith, J. A. P., Everson, R. W., Ramirez-Ruiz, E., et al. 2020, *arXiv e-prints*, arXiv:2011.06630, <https://arxiv.org/abs/2011.06630>
- Maeder, A., & Meynet, G. 2000, *ARA&A*, 38, 143, doi: [10.1146/annurev.astro.38.1.143](https://doi.org/10.1146/annurev.astro.38.1.143)
- Marcolino, W. L. F., Bouret, J. C., Martins, F., et al. 2009, *A&A*, 498, 837, doi: [10.1051/0004-6361/200811289](https://doi.org/10.1051/0004-6361/200811289)
- Mason, B. D., Hartkopf, W. I., Gies, D. R., Henry, T. J., & Helsel, J. W. 2009, *AJ*, 137, 3358, doi: [10.1088/0004-6256/137/2/3358](https://doi.org/10.1088/0004-6256/137/2/3358)
- Meynet, G., & Maeder, A. 2000, *A&A*, 361, 101
- Murphy, S. J., Joyce, M., Bedding, T. R., White, T. R., & Kama, M. 2021, *MNRAS*, 502, 1633, doi: [10.1093/mnras/stab144](https://doi.org/10.1093/mnras/stab144)
- Neo, S., Miyaji, S., Nomoto, K., & Sugimoto, D. 1977, *PASJ*, 29, 249
- Neuhäuser, R., Gießler, F., & Hambaryan, V. V. 2020, *MNRAS*, 498, 899, doi: [10.1093/mnras/stz2629](https://doi.org/10.1093/mnras/stz2629)
- Oda, T., Hino, M., Muto, K., Takahara, M., & Sato, K. 1994, *Atomic Data and Nuclear Data Tables*, 56, 231, doi: [10.1006/adnd.1994.1007](https://doi.org/10.1006/adnd.1994.1007)
- Packet, W. 1981, *A&A*, 102, 17
- Paxton, B., Bildsten, L., Dotter, A., et al. 2011, *ApJS*, 192, 3, doi: [10.1088/0067-0049/192/1/3](https://doi.org/10.1088/0067-0049/192/1/3)
- Paxton, B., Cantiello, M., Arras, P., et al. 2013, *ApJS*, 208, 4, doi: [10.1088/0067-0049/208/1/4](https://doi.org/10.1088/0067-0049/208/1/4)
- Paxton, B., Marchant, P., Schwab, J., et al. 2015, *ApJS*, 220, 15, doi: [10.1088/0067-0049/220/1/15](https://doi.org/10.1088/0067-0049/220/1/15)
- Paxton, B., Schwab, J., Bauer, E. B., et al. 2018, *ApJS*, 234, 34, doi: [10.3847/1538-4365/aaa5a8](https://doi.org/10.3847/1538-4365/aaa5a8)
- Paxton, B., Smolec, R., Gaudy, A., et al. 2019, <https://arxiv.org/abs/1903.01426>
- Pérez, F., & Granger, B. E. 2007, *Computing in Science & Engineering*, 9, 21
- Perna, R., Duffell, P., Cantiello, M., & MacFadyen, A. I. 2014, *ApJ*, 781, 119, doi: [10.1088/0004-637X/781/2/119](https://doi.org/10.1088/0004-637X/781/2/119)

- Podsiadlowski, P. 2003, arXiv e-prints, astro.  
<https://arxiv.org/abs/astro-ph/0303660>
- Pols, O. R., & Marinus, M. 1994, *A&A*, 288, 475
- Pols, O. R., Tout, C. A., Eggleton, P. P., & Han, Z. 1995, *MNRAS*, 274, 964, doi: [10.1093/mnras/274.3.964](https://doi.org/10.1093/mnras/274.3.964)
- Potekhin, A. Y., & Chabrier, G. 2010, *Contributions to Plasma Physics*, 50, 82, doi: [10.1002/ctpp.201010017](https://doi.org/10.1002/ctpp.201010017)
- Przybilla, N., Nieva, M. F., Heber, U., & Butler, K. 2008, *The Astrophysical Journal*, 684, L103, doi: [10.1086/592245](https://doi.org/10.1086/592245)
- Qin, Y., Fragos, T., Meynet, G., et al. 2018, *A&A*, 616, A28, doi: [10.1051/0004-6361/201832839](https://doi.org/10.1051/0004-6361/201832839)
- Renzo, M., Ott, C. D., Shore, S. N., & de Mink, S. E. 2017, *A&A*, 603, A118, doi: [10.1051/0004-6361/201730698](https://doi.org/10.1051/0004-6361/201730698)
- Renzo, M., Zapartas, E., de Mink, S. E., et al. 2019, *A&A*, 624, A66, doi: [10.1051/0004-6361/201833297](https://doi.org/10.1051/0004-6361/201833297)
- Rogers, F. J., & Nayfonov, A. 2002, *ApJ*, 576, 1064, doi: [10.1086/341894](https://doi.org/10.1086/341894)
- Sana, H., de Mink, S. E., de Koter, A., et al. 2012, *Science*, 337, 444, doi: [10.1126/science.1223344](https://doi.org/10.1126/science.1223344)
- Saumon, D., Chabrier, G., & van Horn, H. M. 1995, *ApJS*, 99, 713, doi: [10.1086/192204](https://doi.org/10.1086/192204)
- Schneider, F. R. N., Podsiadlowski, P., Langer, N., Castro, N., & Fossati, L. 2016, *MNRAS*, 457, 2355, doi: [10.1093/mnras/stw148](https://doi.org/10.1093/mnras/stw148)
- Schneider, F. R. N., Podsiadlowski, P., & Müller, B. 2021, *A&A*, 645, A5, doi: [10.1051/0004-6361/202039219](https://doi.org/10.1051/0004-6361/202039219)
- Sota, A., Maíz Apellániz, J., Morrell, N. I., et al. 2014, *ApJS*, 211, 10, doi: [10.1088/0067-0049/211/1/10](https://doi.org/10.1088/0067-0049/211/1/10)
- Spruit, H. C. 2002, *A&A*, 381, 923, doi: [10.1051/0004-6361:20011465](https://doi.org/10.1051/0004-6361:20011465)
- Sweet, P. A. 1950, *MNRAS*, 110, 548, doi: [10.1093/mnras/110.6.548](https://doi.org/10.1093/mnras/110.6.548)
- Tauris, T. M., & Takens, R. J. 1998, *A&A*, 330, 1047
- Tauris, T. M., Kramer, M., Freire, P. C. C., et al. 2017, *ApJ*, 846, 170, doi: [10.3847/1538-4357/aa7e89](https://doi.org/10.3847/1538-4357/aa7e89)
- Tetzlaff, N., Neuhauser, R., Hohle, M. M., & Maciejewski, G. 2010, *MNRAS*, 402, 2369, doi: [10.1111/j.1365-2966.2009.16093.x](https://doi.org/10.1111/j.1365-2966.2009.16093.x)
- Timmes, F. X., & Swesty, F. D. 2000, *ApJS*, 126, 501, doi: [10.1086/313304](https://doi.org/10.1086/313304)
- Townsend, R. 2018, *MESA SDK for Linux*: 20180822, doi: [10.5281/zenodo.2603170](https://doi.org/10.5281/zenodo.2603170)
- van der Walt, S., Colbert, S. C., & Varoquaux, G. 2011, *Computing in Science Engineering*, 13, 22, doi: [10.1109/MCSE.2011.37](https://doi.org/10.1109/MCSE.2011.37)
- van Rensbergen, W., de Greve, J. P., Mennekens, N., Jansen, K., & de Loore, C. 2011, *A&A*, 528, A16, doi: [10.1051/0004-6361/201015596](https://doi.org/10.1051/0004-6361/201015596)
- van Rensbergen, W., De Loore, C., & Jansen, K. 2006, *A&A*, 446, 1071, doi: [10.1051/0004-6361:20053543](https://doi.org/10.1051/0004-6361:20053543)
- van Rensbergen, W., Vanbeveren, D., & De Loore, C. 1996, *A&A*, 305, 825
- Villamariz, M. R., & Herrero, A. 2005, *A&A*, 442, 263, doi: [10.1051/0004-6361:20052848](https://doi.org/10.1051/0004-6361:20052848)
- Vink, J. S., Davies, B., Harries, T. J., Oudmaijer, R. D., & Walborn, N. R. 2009, *A&A*, 505, 743, doi: [10.1051/0004-6361/200912610](https://doi.org/10.1051/0004-6361/200912610)
- Vink, J. S., de Koter, A., & Lamers, H. J. G. L. M. 2000, *A&A*, 362, 295
- . 2001, *A&A*, 369, 574, doi: [10.1051/0004-6361:20010127](https://doi.org/10.1051/0004-6361:20010127)
- Walker, G. A. H., Yang, S., & Fahlman, G. G. 1979, *ApJ*, 233, 199, doi: [10.1086/157381](https://doi.org/10.1086/157381)
- Wang, C., Langer, N., Schootemeijer, A., et al. 2020, *ApJL*, 888, L12, doi: [10.3847/2041-8213/ab6171](https://doi.org/10.3847/2041-8213/ab6171)
- Wheeler, J. C., Lecar, M., & McKee, C. F. 1975, *ApJ*, 200, 145, doi: [10.1086/153771](https://doi.org/10.1086/153771)
- Yoon, S.-C., Langer, N., & Norman, C. 2006, *A&A*, 460, 199, doi: [10.1051/0004-6361:20065912](https://doi.org/10.1051/0004-6361:20065912)
- Zaldarriaga, M., Kushnir, D., & Kollmeier, J. A. 2018, *MNRAS*, 473, 4174, doi: [10.1093/mnras/stx2577](https://doi.org/10.1093/mnras/stx2577)
- Zapartas, E., de Mink, S. E., Justham, S., et al. 2021, *A&A*, 645, A6, doi: [10.1051/0004-6361/202037744](https://doi.org/10.1051/0004-6361/202037744)
- . 2019. <https://arxiv.org/abs/1907.06687>
- Zehe, T., Mugrauer, M., Neuhauser, R., et al. 2018, *Astronomische Nachrichten*, 339, 46, doi: [10.1002/asna.201713383](https://doi.org/10.1002/asna.201713383)